


Quadrature skyrmions in two-dimensionally arrayed parametric resonators

Hiroshi Yamaguchi , Daiki Hatanaka , and Motoki Asano 

NTT Basic Research Laboratories, NTT Corporation, Atsugi, Kanagawa 243-0198, Japan

 (Received 15 March 2023; revised 10 July 2023; accepted 21 September 2023; published 23 October 2023)

Skyrmions are topological solitons in two-dimensional systems and have been observed in various physical systems. Generating and controlling skyrmions in artificial resonator arrays lead to novel acoustic, photonic, and electric devices, but it is a challenge to implement a vector variable with the chiral exchange interaction. Here, we propose to use quadrature variables, where their parametric coupling enables skyrmions to be stabilized. A finite-element simulation indicates that an acoustic skyrmion would exist in a realistic structure consisting of a piezoelectric membrane array.

DOI: [10.1103/PhysRevResearch.5.043076](https://doi.org/10.1103/PhysRevResearch.5.043076)

I. INTRODUCTION

Topological solitons are fundamental excitations observed in various nonlinear systems [1]. The soliton is the phase boundary between two identical but topologically distinguished domains and can be created by spontaneous breaking of translational symmetry [2,3]. One of the most important two-dimensional (2D) solitons is the skyrmion, which has recently attracted much attention especially in the field of ferromagnetic systems [4–10]. A skyrmion has a chiral spin texture and can be induced by an antisymmetric exchange interaction together with a symmetric exchange coupling [11–13]. Skyrmions are stable because of their topological nature and a scheme to control their motion has been proposed [14,15], which may lead to applications of skyrmions in memory [16,17], logic [18], and microwave devices [19–21]. Skyrmions have been shown to appear in numerous physical systems, including quantum Hall systems [22–24] and Bose-Einstein condensate [25–27], and are considered universal phenomena.

The concept of topological insulators has been recently utilized in artificial 2D lattice systems of photonics [28–30], microwave [31], and acoustics [32–34]. The generation and control of skyrmions in these artificial systems are expected to similarly lead to new device and material technologies. However, there have been few reports on the skyrmions generated by spontaneous breaking of translational symmetry in artificial structures. One of the major challenges is how to construct the 2D array of three-component vector variables, with both symmetric and antisymmetric exchange interactions. Various efforts have been made using velocity fields [35] and hybrid displacements [36] in phononics, and also evanescence fields in photonics [37–39], but in the majority of the studies, skyrmionlike textures were created not by

spontaneous symmetry breaking but by interference between external drive signals. Therefore, in those studies, the position of each skyrmion is externally specified and no motion can be induced without changing the external drive. Thus, finding artificial lattice systems with a chiral exchange interaction to induce the spontaneous breaking remains an important research target in the field of skyrmion physics.

In this paper, we propose an alternative approach that utilizes quadrature variables [40], instead of three real-space vector components, in a doubly degenerate 2D harmonic resonator array. This approach has three significant features. First, the skyrmion texture can be generated with the array of only two-component variables. Second, the periodic temporal perturbation, which so far has been discussed mainly in terms of linear Floquet systems [41–43], is also a useful scheme in nonlinear dynamics. Finally, as in the case of topological insulators, the stability of the texture induced by the topological properties can be utilized to develop novel devices and materials technologies. The approach can be applied to various artificial 2D-arrayed resonators, such as microwave circuits and photonic and acoustic metamaterials, holding out the prospect of extensive applications of skyrmion physics to device and material technologies.

II. DOUBLY DEGENERATE 2D LATTICE RESONATOR MODEL

We consider a square array with doubly degenerate resonance modes A and B [Fig. 1(a)]. We introduce a parametric excitation at twice the frequency, $2\omega_0$, where ω_0 is the angular frequency of the two modes. The laboratory-frame Hamiltonian H_0 at a particular site on the lattice is expressed as

$$H_0 = \frac{p_A^2 + p_B^2}{2} + \frac{\omega_0^2}{2}(q_A^2 + q_B^2) + \omega_0^2 \Gamma \cos 2\omega_0 t (q_A^2 - q_B^2) + \frac{\omega_0^2 \alpha}{4}(q_A^2 + q_B^2)^2. \quad (1)$$

Here, $p_k = \dot{q}_k$ ($k = A, B$) is the canonically conjugate momentum of q_k . We have assumed isotropic cubic nonlinearity

Published by the American Physical Society under the terms of the Creative Commons Attribution 4.0 International license. Further distribution of this work must maintain attribution to the author(s) and the published article's title, journal citation, and DOI.

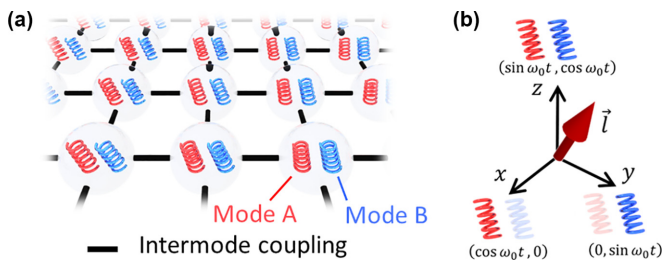


FIG. 1. Conceptual drawing of (a) a doubly degenerate resonator array and (b) a quadrature moment. The x -, y -, and z -aligned \vec{l} quadrature moments correspond to the oscillation states of $(q_A, q_B) = (a_0 \cos \omega_0 t, 0)$, $(0, a_0 \sin \omega_0 t)$, and $(a_0 \sin \omega_0 t, a_0 \cos \omega_0 t)/\sqrt{2}$, respectively.

with a strength of α , and Γ is the parametric excitation intensity. We also assume identical effective masses for both modes and use the unit to make it unity for simplicity. We consider the case that the parametric excitation changes sign between the two orthogonal modes as shown in the third term in (1). This is the essential assumption under which to assign stable parametric oscillation states to z -polarized vector states and the physical implementation will be described later.

The mode variable $q_k(t)$ is expressed as

$$q_k(t) = c_k(t) \cos \omega_0 t + s_k(t) \sin \omega_0 t, \quad (2)$$

under the rotating wave approximation, where the slowly varying cosine and sine oscillation amplitudes, c_k and s_k , are called quadratures. The time-dependent canonical transformation (see Appendix A) leads to new Hamiltonian h_0 expressed as

$$h_0 \sim \frac{\omega_0^2 \Gamma}{4} [(c_A^2 - s_A^2) - (c_B^2 - s_B^2)] + \frac{3\omega_0^2 \alpha}{32} [(c_A^2 + s_A^2) + (c_B^2 + s_B^2)]^2 - \frac{\omega_0^2 \alpha}{8} (c_A s_B - s_A c_B)^2, \quad (3)$$

and the equation of motion is given by $\dot{c}_k = \omega_0^{-1} \partial h_0 / \partial s_k$ and $\dot{s}_k = -\omega_0^{-1} \partial h_0 / \partial c_k$. The steady-state solution, $\dot{c}_k = \dot{s}_k = 0$, corresponds to a local minimum (or maximum) of h_0 [40,44] and consists of four oscillation states, L_{\pm} and R_{\pm} , given by $(c_A, s_A, c_B, s_B) = \sqrt{\Gamma/\alpha}(0, \pm 1, \pm 1, 0)$ and $\sqrt{\Gamma/\alpha}(0, \pm 1, \mp 1, 0)$, i.e.,

$$\begin{aligned} L_{\pm} : q_A(t) &= \pm a_0 \sin \omega_0 t, & q_B(t) &= \pm a_0 \cos \omega_0 t, \\ R_{\pm} : q_A(t) &= \pm a_0 \sin \omega_0 t, & q_B(t) &= \mp a_0 \cos \omega_0 t, \end{aligned} \quad (4)$$

where $a_0 = \sqrt{\Gamma/\alpha}$ is the parametric oscillation amplitude (see Appendix A). As will be shown later, L_{\pm} and R_{\pm} are clockwise and anticlockwise circularly polarized oscillation states, where the sign corresponds to the parametric oscillation phases. We here assumed no damping for simplicity, but this Hamiltonian picture provides a good approximation also for a realistic case that has a finite damping. This is because it assumes that the parametric actuation Γ is sufficiently larger than the oscillation threshold determined by the damping. The two modes A and B are equally mixed with a $\pi/2$ phase

difference in these steady states and form stable circularly polarized oscillations.

Next, we define a three-component quadrature moment using four variables, c_A, s_A, c_B, s_B . We employ two definitions in which the moment is linear with respect to the quadratures,

$$\begin{aligned} \vec{l} &= (l_x, l_y, l_z) \equiv \left(c_A, s_B, \frac{s_A + c_B}{\sqrt{2}} \right), \\ \vec{r} &= (r_x, r_y, r_z) \equiv \left(c_A, s_B, \frac{s_A - c_B}{\sqrt{2}} \right). \end{aligned} \quad (5)$$

These definitions do not satisfy the Poisson-bracket algebra of angular momentum but are ideal for our purpose of creating skyrmions. We can easily confirm that the four parametric oscillation states L_{\pm} and R_{\pm} correspond to z -polarized quadrature moments [see Fig. 1(b) and Appendix A]. It should be noted that h_0 is invariant under the replacement, $(c_A, s_B) \rightarrow (s_B, -c_A)$, which corresponds to a $\pi/2$ rotation in the xy plane as confirmed by the definition (5).

Next, as a preliminary step before discussing the detailed device structures, we mathematically construct a Dzyaloshinskii–Moriya (DM) interaction for the quadrature moments as well as the symmetric exchange coupling. We then numerically confirm that it leads to a skyrmion texture under parametric excitation. The symmetric exchange coupling between two nearest-neighbor sites is given by the isotropic interaction, $h_{\text{EX}} = -g_s(q_{1A}q_{2A} + q_{1B}q_{2B})$ with $g_s > 0$, where the indexes 1 and 2 specify adjacent site positions. The rotating wave approximation leads to

$$h_{\text{EX}} \sim -\frac{g_s}{2}(c_{1A}c_{2A} + s_{1A}s_{2A} + c_{1B}c_{2B} + s_{1B}s_{2B}). \quad (6)$$

Then, we introduce a chiral exchange interaction to create a skyrmion texture. The DM interaction between two nearest-neighbor magnetic moments \vec{m}_1 and \vec{m}_2 is expressed as $h_{\text{DM}} = g_{\text{DM}} \vec{n}_{12} \cdot (\vec{m}_1 \times \vec{m}_2)$ [11,12]. Here, \vec{n}_{12} is the DM vector and it can be chosen as, for example, a unit vector directed from site 1 to site 2 for generating a Bloch-type skyrmion [45]. For a resonator pair parallel to the x axis, $\vec{n}_{12} = e_x \equiv (1, 0, 0)$ and $h_{\text{DM}-x} = g_{\text{DM}}(m_1^y m_2^z - m_1^z m_2^y)$. Similarly, for the y axis, $\vec{n}_{12} = e_y \equiv (0, 1, 0)$ and $h_{\text{DM}-y} = g_{\text{DM}}(m_1^z m_2^x - m_1^x m_2^z)$. If we replace \vec{m} by \vec{l} or \vec{r} , we obtain the DM interaction from Eq. (5) as follows:

$$\begin{aligned} h_{\text{DM}-x}^{(L/R)} &= \frac{g_{\text{DM}}}{\sqrt{2}} [s_{1B}s_{2A} - s_{1A}s_{2B} \pm (s_{1B}c_{2B} - c_{1B}s_{2B})], \\ h_{\text{DM}-y}^{(L/R)} &= \frac{g_{\text{DM}}}{\sqrt{2}} [s_{1A}c_{2A} - c_{1A}s_{2A} \pm (c_{1B}c_{2A} - c_{1A}c_{2B})]. \end{aligned} \quad (7)$$

Here, the plus (minus) sign corresponds to the L (R) mode. The terms including the products of sine and cosine quadratures need a phase-shifted coupling. We can eliminate these terms by making a linear combination,

$$\begin{aligned} h_{\text{DM}-x} &= \frac{h_{\text{DM}-x}^{(L)} + h_{\text{DM}-x}^{(R)}}{\sqrt{2}} = g_{\text{DM}} [s_{1B}s_{2A} - s_{1A}s_{2B}], \\ h_{\text{DM}-y} &= \frac{h_{\text{DM}-y}^{(L)} - h_{\text{DM}-y}^{(R)}}{\sqrt{2}} = g_{\text{DM}} [c_{1B}c_{2A} - c_{1A}c_{2B}]. \end{aligned} \quad (8)$$

For a $\pi/2$ rotation of the quadrature moments, i.e., $(c_A, s_B) \rightarrow (s_B, -c_A)$, this interaction sustains symmetry

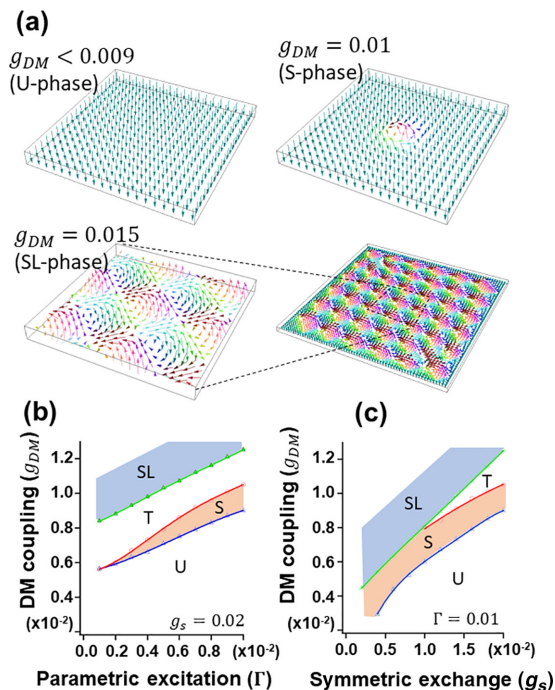


FIG. 2. (a) Calculated spatial distribution of $\vec{l}_{(i,j)}$ for various g_{DM} with $g_s = 0.02$, $\Gamma = 0.01$, and $n_r = 2$. The color corresponds to the direction and amplitude of quadrature moments, where RGB color intensities represent l_z , l_x , and l_y components, respectively. (b),(c) Phase diagrams of unstable (U), single skyrmion (S), transition (T), and skyrmion lattice (SL) regions for various g_{DM} , Γ , and g_s .

for $L\pm$ states and antisymmetry for $R\pm$. This difference induces different skyrmion textures, Bloch skyrmions for $L\pm$ but antiskyrmions for $R\pm$, as shown below. Although this DM interaction seems artificial, we will later find that it can be implemented in a realistic mechanical resonator array.

III. NUMERICAL CALCULATION OF SKYRMION TEXTURES

We then performed a numerical calculation to find a stable texture of quadrature moments. Hereafter, we will employ the unit $\omega_0 = 1$ for simplicity. From (6) and (8), the full

interaction Hamiltonian is given by

$$\begin{aligned}
 h_{\text{int}} = & -\frac{gS}{2} \sum_{i,j,k=A,B} (c_{(i,j)k}c_{(i+1,j)k} + c_{(i,j)k}c_{(i,j+1)k}) \\
 & + s_{(i,j)k}s_{(i+1,j)k} + s_{(i,j)k}s_{(i,j+1)k}) \\
 & + g_{DM} \sum_{i,j} (s_{(i,j)B}s_{(i+1,j)A} - s_{(i,j)A}s_{(i+1,j)B} \\
 & + c_{(i,j)B}c_{(i,j+1)A} - c_{(i,j)A}c_{(i,j+1)B}). \quad (9)
 \end{aligned}$$

Here, the suffix (i, j) denotes the site position in a 2D square array. A stable solution that minimizes the total Hamiltonian was calculated starting from the initial texture, in which an $L+$ domain of radius n_r is surrounded by an $L-$ domain. The time evolution was calculated using the Runge-Kutta method after applying a small perturbation to the obtained minimum-energy solution. This test confirms the local stability of obtained solutions and the details are shown in the next section. We also compared the textures using various initial guesses, changing the position, radius, and shape of domains, and confirmed that no significant change in the obtained phase diagram was observed.

The calculated textures using 64×64 unit cells for various g_{DM} are shown in Fig. 2(a) in the form of the 2D distribution of $\vec{l}_{(i,j)}$. When g_{DM} is smaller than the onset value for skyrmion formation ($g_{DM} < 0.009$), the skyrmion texture is unstable (U phase) and all of the moments are directed downward, i.e., $\vec{l}_{(i,j)} = (0, 0, -\sqrt{2}a_0)$ for all (i, j) . Above the onset, a single skyrmion texture forms (S phase) whose structure is nearly independent of g_{DM} . The magnified texture is shown in Fig. 3(a) for $g_{DM} = 0.095$. As discussed in the next section, the calculated time evolution shows that the texture is metastable because a sufficiently large perturbation of the oscillation amplitude destabilizes it. Above the upper bound ($g_{DM} \geq 0.0105$), the transition to an extended texture (T phase) emerges, where the skyrmion deconfines and occupies the whole lattice in an extremely anisotropic shape, and finally the texture of a skyrmion lattice (SL phase) forms at $g_{DM} \geq 0.0125$. This texture remains stable against the perturbation in contrast to the metastable S phase.

We then examined the topological features of the obtained textures by calculating the skyrmion number. Instead of the generally used expression for a continuous system, $S = \int \vec{n} \cdot (\partial_x \vec{n} \times \partial_y \vec{n}) dx dy / 4\pi$, summing up the solid angles formed by all sets of three adjacent pseudomoments makes

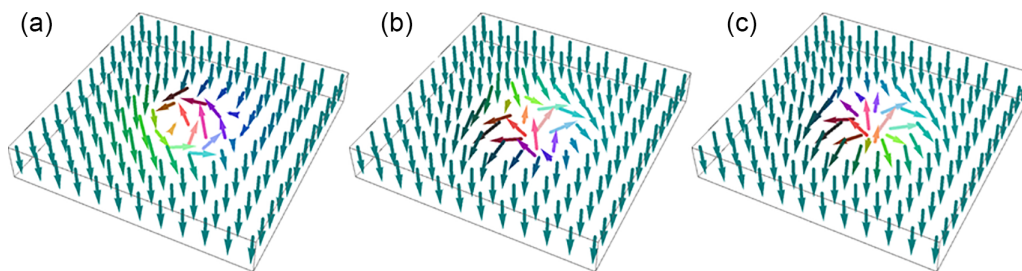


FIG. 3. Birds-eye views of calculated textures for (a) Bloch skyrmion, (b) antiskyrmion, and (c) Néel skyrmion, plotting $\vec{l}_{(i,j)}$ for (a), and $\vec{r}_{(i,j)}$ for (b) and (c). The DM vector is $\vec{n}_{12} = e_x$ for the x axis and e_y for the y axis in (a) and (b), whereas it is e_y for the x axis and $-e_x$ for the y axis in (c). For all plots, $g_s = 0.02$, $\Gamma = 0.01$, $g_{DM} = 0.095$, and $n_r = 2$.

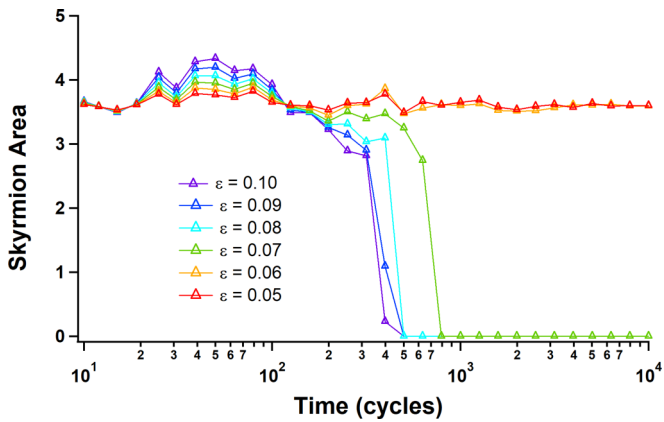


FIG. 4. Time evolution of skyrmion area with a typical texture [Fig. 3(a)]. The unit of time is the oscillation cycle, i.e., $\omega_0 t / 2\pi$.

the skyrmion number unity as expected for a topological soliton (see Appendix B). Figures 2(b) and 2(c) show the phase diagrams of the texture as a function of Γ , g_s , and g_{DM} . The S - U boundary in Fig. 2(c) suggests that the parameter g_{DM}^2/g_s governs the transition [45]. We can see that the skyrmion and its lattice textures occur over a wide parameter range. Similar calculations using \bar{r} generated an antiskyrmion texture [Fig. 3(b)]. We also generated a Néel-type skyrmion by using the different DM vector, $\bar{n}_{12} = e_y$, for the x axis and $-e_x$ for the y axis [Fig. 3(c) and Appendix C] [46], indicating that various skyrmion textures are possible.

IV. TEXTURE STABILITY

To investigate the stability of the skyrmion solution, we performed a two-step calculation. First, a solution providing the local minimum of h_0 is calculated. Then, small perturbations are added to the quadratures,

$$c_{(i,j)k} \rightarrow c_{(i,j)k} + \Delta c_{(i,j)k}, \quad s_{(i,j)k} \rightarrow s_{(i,j)k} + \Delta s_{(i,j)k},$$

at $t = 0$, and their time evolution is calculated, where the equations of motion are modified to include the effect of weak

damping,

$$\dot{c}_k = \omega_0^{-1} \frac{\partial h_0}{\partial s_k} - \frac{\omega_0 Q}{2} c_k, \quad \dot{s}_k = -\omega_0^{-1} \frac{\partial h_0}{\partial c_k} - \frac{\omega_0 Q}{2} s_k,$$

where Q is the quality factor of the resonator (assumed to be 10^4). Figure 4 plots the time evolution of the skyrmion area, i.e., the average number of positively z -polarized quadrature moments for different amounts of Gaussian perturbation $\varepsilon = \sqrt{(\Delta c_{(i,j)k})^2} = \sqrt{(\Delta s_{(i,j)k})^2}$. The texture is maintained for $\varepsilon \leq 6\%$, but it disappears for $\varepsilon \geq 7\%$. This result confirms that the skyrmion is locally stable, but a large perturbation breaks the texture, causing the system to fall into the lowest-energy single ferromagnetic domain. Therefore, the isolated skyrmion (\mathcal{S} phase) is not energetically lowest but metastable, corresponding to the locally minimum quasienergy state.

We also discuss the robustness of skyrmions against the resonator inhomogeneity. We especially examine the influence of resonance frequency fluctuation, which is one of the most common inhomogeneities induced by the inaccuracy in device fabrication. Here, let us introduce a frequency detuning $\delta_{(i,j)} = (\omega_{0(i,j)} - \omega_0)/\omega_0$ for each resonator obeying a Gaussian distribution, where $\omega_{0(i,j)}$ is the resonance frequency at site (i, j) . The steady-state textures for various fluctuation $\sigma = \sqrt{\delta_{(i,j)}^2}$ are calculated by solving the equation of motion with a finite damping (Fig. 5). When $\sigma \leq 0.02$, the skyrmion texture remains stable against the frequency fluctuation. For a larger σ , skyrmion-shaped excitations were randomly generated, indicating instability. This corresponds to the fact that the ferromagnetic ordering is not maintained when the fluctuation is larger than g_s . Nonetheless, since fabrication tolerances of 2% are generally obtained in real device fabrication [47], it should be possible to demonstrate skyrmions in actual devices.

V. IMPLEMENTATION USING MEMBRANE RESONATORS

Next, let us discuss a realistic device model implementing the DM interaction. Although our concept can be applied to various physical systems, we here envision an implementation in a nanomechanical resonator array consisting of coupled

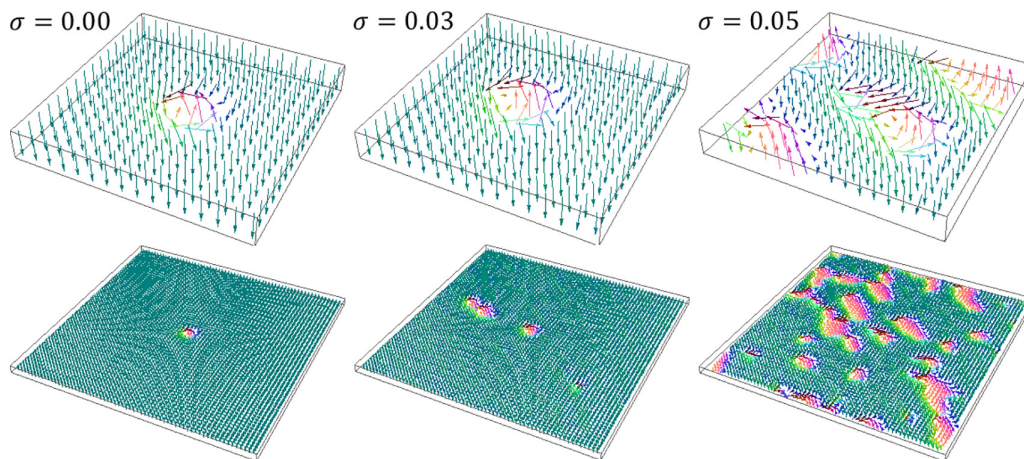


FIG. 5. Calculated textures when frequency fluctuations with different fluctuation variances σ are applied. $g_s = 0.02$, $\Gamma = 0.01$, $g_{DM} = 0.095$, and damping $1/Q \sim 10^{-4}$.

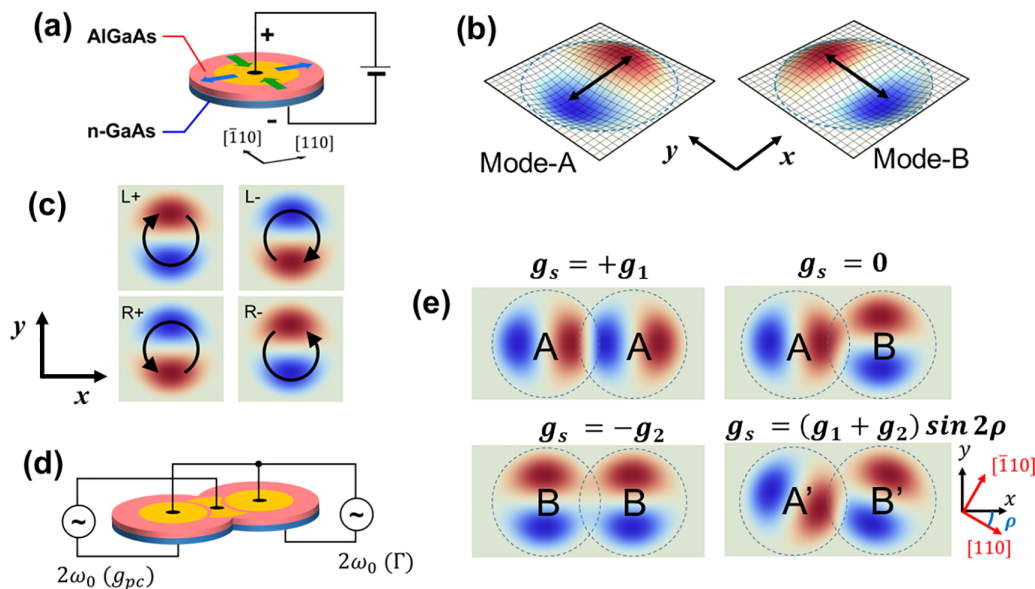


FIG. 6. (a) Schematic drawing of circular electromechanical membrane resonator and (b) two vibration modes, *A* and *B*. (c) Four parametric oscillation states. *L/R* indicates the circular polarization and *+/-* indicates the oscillation phase. (d) Schematic drawing of the device configuration. An alternating voltage at $2\omega_0$ is applied to the center electrode for parametric excitation and to the junction electrode for parametric coupling. (e) Schematic illustration of the coupling constants. Two different constants, g_1 and g_2 , are introduced and the coupling between the *A* and *B* modes is established by misaligning the piezoelectric and membrane axes.

piezoelectric circular membranes [48,49]. The unit structure, shown in Fig. 6(a), has doubly degenerate modes, *A* and *B* [Fig. 6(b)], and the circular edge is fixed. Because of its d_{31} piezoelectric component [47,50,51], the applied voltage induces a different sign of tension between two orthogonal directions, $[110]$ and $[1\bar{1}0]$ [Fig. 6(a) and Appendix D]. This anisotropy changes the sign of parametric excitation required to derive the third term in Eq. (1) and enables four circularly polarized parametric oscillation states to be excited [Eq. (4) and Fig. 6(c)].

The symmetric exchange coupling, Eq. (6), is mediated by the elastic coupling through the overlap [Fig. 6(d)], where we

need to consider two coupling constants, g_1 and g_2 [Fig. 6(e)]. A comparison of (8) with (6) indicates that an *A-B* mixing interaction is required to induce the quadrature DM interaction. Accordingly, we employed a misalignment between the piezoelectric and membrane-lattice axes [Fig. 6(e)]. After redefining the even-site resonator amplitude with reversed sign, the mixing term is given by

$$[h_{EX-\rho}]_{AB} \sim -\frac{g_s}{2} \sin 2\rho (c_{1B}c_{2A} + s_{1B}s_{2A} - c_{1A}c_{2B} - s_{1A}s_{2B}). \tag{10}$$

Here, ρ is the misalignment angle and $g_s = (g_1 + g_2)/2$ (see the full expression in Appendix E). Although the *A-B* mixing

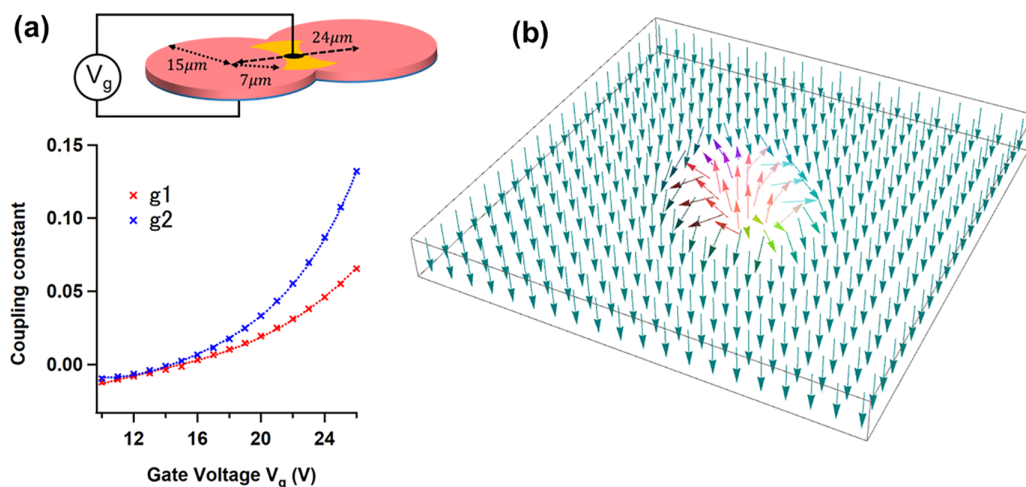


FIG. 7. (a) Calculated static coupling constants as a function of gate voltage using FEM for the geometry indicated at the top. The resonator thickness is 100 nm and the elastic and piezoelectric parameters of GaAs are used in the calculation. (b) The texture of Néel skyrmion in terms of $\vec{r}_{(i,j)}$ calculated from the parameters given by FEM and using a voltage modulation of $4.0 V_{rms}$ and $\rho = 20^\circ$.

is introduced, this interaction is identical between the x and y axes and unable to introduce the chiral interaction. This is reasonable because both $c'_k s$ and $s'_k s$ are coupled in the same way through $q'_k s$. To induce chirality, we need to introduce an interaction that independently couples $c'_k s$ and $s'_k s$. This can be done by using the parametric coupling proposed for another topological system [30]. We here show that combining this parametric coupling together with the parametric excitation induces a stable skyrmion texture.

A modulation, $g_S(t) = g_{S0} + g_{pc} \cos(2\omega_0 t)$, leads to the following AB mixing exchange interaction:

$$[h_{pc}]_{AB} = -\frac{g_{pc}}{4} \sin 2\rho (c_{1B}c_{2A} - s_{1B}s_{2A} - c_{1A}c_{2B} + s_{1A}s_{2B}). \quad (11)$$

Here, the signs of s_k are opposite to those in (10) so that applying a differently signed $2\omega_0$ modulation between the x - and y -axis coupling creates a chiral interaction. This can easily be done in our device configuration by applying opposite signed alternating voltages. The total AB mixing part becomes

$$[h_{EX-\rho} + h_{pc}]_{AB} = -\sin 2\rho \left[\frac{g_+}{2} (c_{1B}c_{2A} - c_{1A}c_{2B}) + \frac{g_-}{2} (s_{1B}s_{2A} - s_{1A}s_{2B}) \right]. \quad (12)$$

Here, $g_+ = g_{S0} + \frac{g_{pc}}{2}$, $g_- = g_{S0} - \frac{g_{pc}}{2}$. In the case of $g_{pc} = -2g_{S0}$ for the x axis and $+2g_{S0}$ for the y axis, we obtain

$$[h_{EX-\rho} + h_{pc}]_{AB;x} = -g_{S0} \sin 2\rho (s_{1B}s_{2A} - s_{1A}s_{2B}),$$

$$[h_{EX-\rho} + h_{pc}]_{AB;y} = -g_{S0} \sin 2\rho (c_{1B}c_{2A} - c_{1A}c_{2B}). \quad (13)$$

These equations are identical to the DM interaction, Eq. (8). Therefore, the combined effects of the misaligned piezoelectric axis and $2\omega_0$ modulation of the symmetric exchange coupling can induce the chiral interaction required to form a skyrmion. We can also generate a Néel-type DM interaction by changing the sign of the parametric coupling (see Appendix C), so that the kind of creating skyrmion can be externally controlled.

We performed numerical calculations to verify the above findings. First, we performed a simulation using the finite element method (FEM) using COMSOL Multiphysics® to numerically determine the coupling constants (see Appendix D). Figure 7(a) shows the calculated coupling constant between two adjacent membrane resonators as a function of gate voltage on the overlap area. For an offset bias voltage of 20 V, we can successfully obtain a Néel-type texture as shown in Fig. 7(b).

VI. CONCLUSION

In conclusion, we proposed an approach to generating various skyrmions that utilizes four quadrature variables in 2D parametric resonator arrays. This numerical demonstration of skyrmions is in systems formed by only two dynamical variables through temporal periodic perturbation. The concept can be applied to other kinds of parametric resonator, including photonic and microwave resonator arrays.

ACKNOWLEDGMENTS

The authors would like to thank H. Okamoto for his continuous encouragements. This work was partially supported by JSPS KAKENHI Grant-in-Aid for Scientific Research (JP21H05020 and JP23H05463).

APPENDIX A: DERIVATION OF PARAMETRIC OSCILLATION STATES

We start from the single resonator Hamiltonian (1),

$$H_0 = \frac{P_A^2 + P_B^2}{2} + \frac{\omega_0^2}{2} (q_A^2 + q_B^2) + \omega_0^2 \Gamma \cos 2\omega_0 t (q_A^2 - q_B^2) + \frac{\omega_0^2 \alpha}{4} (q_A^2 + q_B^2)^2.$$

Using the generator F of the time-dependent canonical transformation for a rotating frame,

$$F(q_A, Q_A, q_B, Q_B, t) = \sum_{k=A,B} \left(\frac{\omega_0 q_k^2}{2 \tan \omega_0 t} - \frac{\sqrt{\omega_0} q_k Q_k}{\sin \omega_0 t} + \frac{Q_k^2}{2 \tan \omega_0 t} \right), \quad p_k = \frac{\partial F}{\partial q_k}, \quad P_k = -\frac{\partial F}{\partial Q_k}, \quad h_0 = H_0 + \frac{\partial F}{\partial t},$$

we obtain

$$q_k = \omega_0^{-1/2} (P_k \sin \omega_0 t + Q_k \cos \omega_0 t), \quad p_k = \omega_0^{1/2} (P_k \cos \omega_0 t - Q_k \sin \omega_0 t),$$

$$h_0 \sim \frac{\omega_0 \Gamma}{4} (Q_A^2 - P_A^2 - Q_B^2 + P_B^2) + \frac{3\alpha}{32} (P_A^2 + Q_A^2 + P_B^2 + Q_B^2)^2 - \frac{\alpha}{8} (Q_A P_B - P_A Q_B)^2.$$

Here, we neglect the rapidly oscillating terms. The canonical equations of motion become

$$\dot{Q}_k = \frac{\partial h_0}{\partial P_k}, \quad \dot{P}_k = -\frac{\partial h_0}{\partial Q_k}.$$

We can obtain (3) and the equation of motion

$$\dot{c}_k = \omega_0^{-1} \frac{\partial h_0}{\partial s_k}, \quad \dot{s}_k = -\omega_0^{-1} \frac{\partial h_0}{\partial c_k}$$

by using $c_k = \omega_0^{-1/2} Q_k$ and $s_k = \omega_0^{-1/2} P_k$. To find the steady-state solution, we define c , s , θ_c , and θ_s as

$$c_A = c \cos \theta_c, \quad s_B = c \sin \theta_c,$$

$$s_A = s \cos \theta_s, \quad c_B = s \sin \theta_s.$$

Then,

$$h_0 = \omega_0^2 \left[\frac{\Gamma}{4} (c^2 - s^2) + \frac{3\alpha}{32} (c^2 + s^2)^2 - \frac{\alpha}{32} (c^2 \sin 2\theta_c - s^2 \sin 2\theta_s)^2 \right].$$

We assume that $\Gamma > 0$ and $\alpha > 0$; then $h_0 \rightarrow +\infty$ for $c, s \rightarrow \pm\infty$. Therefore, a stable solution is found at the minimum of h_0 . For given c and s , the last term becomes smallest when

$$\begin{aligned} \sin 2\theta_c &= \pm 1, & \sin 2\theta_s &= 0 \quad (c^2 \geq s^2), \\ \sin 2\theta_c &= 0, & \sin 2\theta_s &= \pm 1 \quad (c^2 \leq s^2). \end{aligned}$$

Then,

$$\begin{aligned} h_0 &= \omega_0^2 \left[\frac{\Gamma}{4}(c^2 - s^2) + \frac{3\alpha}{32}(c^2 + s^2)^2 - \frac{\alpha}{32}c^4 \right] \quad (c^2 \geq s^2), \\ h_0 &= \omega_0^2 \left[\frac{\Gamma}{4}(c^2 - s^2) + \frac{3\alpha}{32}(c^2 + s^2)^2 - \frac{\alpha}{32}s^4 \right] \quad (c^2 \leq s^2). \end{aligned}$$

When $c^2 \geq s^2$, the coefficients of c^4 and c^2 are always positive so that the energy has a minimum value when $c = 0$ and $s = 0$. Therefore, $c^2 < s^2$. Then, $c = 0$ and

$$h_0 = \omega_0^2 \left[\frac{\alpha}{16}s^4 - \frac{\Gamma}{4}s^2 \right] = \frac{\alpha\omega_0^2}{16} \left[\left(s^2 - \frac{2\Gamma}{\alpha} \right)^2 - \frac{4\Gamma^2}{\alpha^2} \right].$$

This expression reaches a minimum at

$$s = \pm\sqrt{2}a_0, \quad a_0 = \sqrt{\frac{\Gamma}{\alpha}}.$$

On the other hand, from $\sin 2\theta_s = \pm 1$, we have $\theta_s = \frac{\pi}{4}, \frac{3\pi}{4}, \frac{5\pi}{4}, \frac{7\pi}{4}$. Thus, the four solutions are

$$c_A = 0, \quad s_B = 0, \quad s_A = s \cos \theta_s = \pm a_0, \quad c_B = s \sin \theta_s = \pm a_0.$$

Here, the sign \pm can be chosen independently for s_A and c_B . The above corresponds to the solutions given by (4). The expression using the quadrature moments \vec{l} and \vec{r} is shown in Table I, indicating that $L\pm$ and $R\pm$ correspond to z -polarized quadrature moments.

APPENDIX B: CALCULATION OF SKYRMION NUMBER

The skyrmion number of a continuous system is calculated using the formula

$$S = \frac{\int \vec{n} \cdot (\partial_x \vec{n} \times \partial_y \vec{n}) dx dy}{4\pi}.$$

Here, \vec{n} is the unit vector of the moment. The discrete version is given by

$$\begin{aligned} S &= \frac{\sum_{i,j} \vec{\eta}(i,j) \cdot (\Delta_x \vec{\eta}(i,j) \times \Delta_y \vec{\eta}(i,j))}{4\pi} \\ &= \frac{\sum_{i,j} \vec{\eta}(i,j) \cdot (\vec{\eta}(i+1,j) \times \vec{\eta}(i,j+1))}{4\pi}. \end{aligned} \tag{14}$$

TABLE I. Quadrature moments for four parametric oscillation states, $L\pm$ and $R\pm$.

	(l_x, l_y, l_z)	(r_x, r_y, r_z)
$L\pm$	$(0, 0, \pm\sqrt{2}a_0)$	$(0, 0, 0)$
$R\pm$	$(0, 0, 0)$	$(0, 0, \pm\sqrt{2}a_0)$

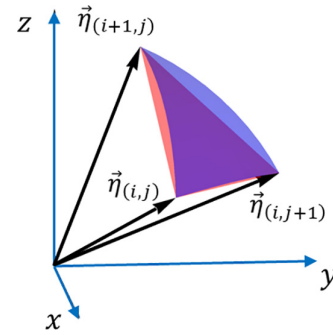


FIG. 8. Schematic drawing of the solid angle, i.e., the area of curved surface colored in blue, calculated by L'Huilier's formula. The red triangle is the area calculated using the formula (14). The area of the flat triangle colored in red is smaller than that of the curved surface in blue, providing the smaller skyrmion number of 0.65.

Here, $\vec{\eta}(i,j) \equiv \vec{l}(i,j)/|\vec{l}(i,j)|$ (in the case of \vec{l}) is the unit vector of the quadrature moment and $\Delta_x \vec{\eta}(i,j) = \vec{\eta}(i+1,j) - \vec{\eta}(i,j)$ and $\Delta_y \vec{\eta}(i,j) = \vec{\eta}(i,j+1) - \vec{\eta}(i,j)$ are nearest-neighbor differences. We obtained $C = 0.65$ for an isolated skyrmion [$g_{DM} = 0.01$ in Fig. 2(a)]. This is smaller than the ideal value of unity because of the discreteness of the lattice. By using L'Huilier's formula, which determines the solid angle Ω (Fig. 8) from three unit vectors,

$$\begin{aligned} \Omega &= 4\eta \tan^{-1} \sqrt{\tan \frac{\theta_s}{2} \tan \frac{\theta_s - \theta_A}{2} \tan \frac{\theta_s - \theta_B}{2} \tan \frac{\theta_s - \theta_C}{2}}, \\ \theta_s &= \frac{\theta_A + \theta_B + \theta_C}{2}, \end{aligned}$$

where $\theta_A, \theta_B,$ and θ_C are three interior angles formed by the three unit vectors, we can calculate the total solid angle covered by the quadrature moments for all the sets of

$$\begin{aligned} &(\cos \theta_A, \cos \theta_B, \cos \theta_C) \\ &= (\vec{\eta}(i+1,j) \cdot \vec{\eta}(i,j+1), \vec{\eta}(i,j) \cdot \vec{\eta}(i+1,j), \vec{\eta}(i,j) \cdot \vec{\eta}(i,j+1)), \\ \eta &= \text{sgn}[(\vec{\eta}(i+1,j) \times \vec{\eta}(i,j+1)) \cdot \vec{\eta}(i,j)], \end{aligned}$$

and

$$\begin{aligned} &(\cos \theta_A, \cos \theta_B, \cos \theta_C) \\ &= (\vec{\eta}(i-1,j) \cdot \vec{\eta}(i,j-1), \vec{\eta}(i,j) \cdot \vec{\eta}(i-1,j), \vec{\eta}(i,j) \cdot \vec{\eta}(i,j-1)), \\ \eta &= \text{sgn}[(\vec{\eta}(i-1,j) \times \vec{\eta}(i,j-1)) \cdot \vec{\eta}(i,j)]. \end{aligned}$$

The sum of Ω for the obtained isolated skyrmion solution becomes 4π , showing that the pseudomoment covers the surface of a unit sphere.

APPENDIX C: NÉEL-TYPE DM INTERACTIONS

To generate a Néel-type skyrmion, $\vec{n}_{12} = (0, 1, 0)$ and $h_{DM} = g_{DM}(m_1^z m_2^x - m_1^x m_2^z)$ for a resonator pair aligned to the x axis, and $\vec{n}_{12} = (-1, 0, 0)$ and $h_{DM} = g_{DM}(-m_1^y m_2^z + m_1^z m_2^y)$ for a resonator pair aligned to the y axis. If we replace \vec{m} by \vec{l} , we obtain the quadrature DM interaction as

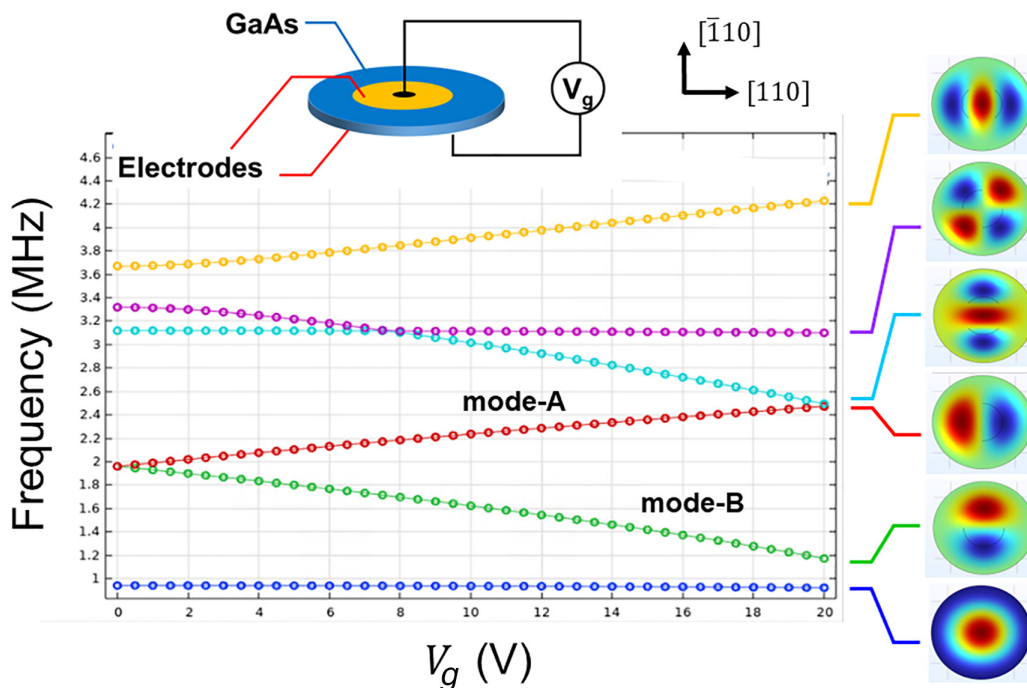


FIG. 9. Calculated flexural mode frequencies for a circular membrane GaAs resonator as a function of gate voltage applied between the top and bottom electrodes. The top electrode and membrane radius are 6 μm and 15 μm , respectively, and the bottom electrode covers the back surface of the membrane. We set fixed boundary conditions along the edge of the membrane. We used two specific modes (plots colored in red and green) for the numerical calculation.

follows:

$$h_{\text{DM}-x}^{(L)} = \frac{g_{\text{DM}}}{\sqrt{2}} [s_{1A}c_{2A} - c_{1A}s_{2A} + c_{1B}c_{2A} - c_{1A}c_{2B}],$$

$$h_{\text{DM}-y}^{(L)} = -\frac{g_{\text{DM}}}{\sqrt{2}} [s_{1B}s_{2A} - s_{1A}s_{2B} + s_{1B}c_{2B} - c_{1B}s_{2B}].$$

Similarly, we can define the DM interaction for \bar{r} as

$$h_{\text{DM}-x}^{(R)} = \frac{g_{\text{DM}}}{\sqrt{2}} [s_{1A}c_{2A} - c_{1A}s_{2A} - c_{1B}c_{2A} + c_{1A}c_{2B}],$$

$$h_{\text{DM}-y}^{(R)} = -\frac{g_{\text{DM}}}{\sqrt{2}} [s_{1B}s_{2A} - s_{1A}s_{2B} - s_{1B}c_{2B} + c_{1B}s_{2B}].$$

We can eliminate the sine and cosine mixing terms by making a linear combination,

$$h_{\text{DM}-x}^{(\text{Néel})} = \frac{h_{\text{DM}-x}^{(R)} - h_{\text{DM}-x}^{(L)}}{\sqrt{2}} = -g_{\text{DM}} [c_{1B}c_{2A} - c_{1A}c_{2B}],$$

$$h_{\text{DM}-y}^{(\text{Néel})} = \frac{h_{\text{DM}-y}^{(R)} + h_{\text{DM}-y}^{(L)}}{\sqrt{2}} = -g_{\text{DM}} [s_{1B}s_{2A} - s_{1A}s_{2B}].$$

In contrast to (8), which creates a Bloch-type skyrmion, these interaction Hamiltonians create the Néel-type skyrmion for $R\pm$ as shown in Fig. 3(c).

APPENDIX D: PIEZOELECTRIC RESONANT FREQUENCY MODULATION

To obtain quadrature DM interaction (8), we assumed that the parametric frequency shift has opposite signs between two modes. To confirm the feasibility of this assumption, we calculated the flexural mode frequency as a function of

DC gate voltage for a single membrane resonator using a finite element method (FEM). The calculation is performed using COMSOL Multiphysics® by discretizing the full three-dimensional geometry of the single and coupled membranes with 55 460 tetrahedral elements with a minimum size of 6 nm. A second-order partial differential equation was applied with fixed constraints at the circular edge of the membrane(s). As a standard measure to evaluate the quality of meshes, the skewness is calculated giving the average value of 0.845, which is large enough to support the mesh quality. Figure 9 shows the results, which confirm that the voltage-induced frequency shift has an opposite sign between the piezoelectric axes (modes B and C). We can also confirm that a frequency shift of about 1.5% is obtained at $V_g = 1$ V, which is large enough to induce the required parametric excitation of $\Gamma = 0.01$.

APPENDIX E: FULL EXPRESSION OF INTERACTION HAMILTONIAN IN COUPLED MEMBRANE MODEL

First, let us start to derive the symmetric exchange coupling with a misaligned piezoelectric axis. Figure 10 shows the displacement distribution of x - and y -aligned linearly polarized modes in two coupled membrane resonators with different couplings g_1 and g_2 .

Denoting the tilt angle as ρ , the displacements of the two modes A and B aligned to two piezoelectric axes are

$$q_{1A} = \hat{q}_{1A} \cos \rho - \hat{q}_{1B} \sin \rho, \quad q_{1B} = \hat{q}_{1A} \sin \rho + \hat{q}_{1B} \cos \rho,$$

$$q_{2A} = \hat{q}_{2A} \cos \rho - \hat{q}_{2B} \sin \rho, \quad q_{2B} = \hat{q}_{2A} \sin \rho + \hat{q}_{2B} \cos \rho.$$

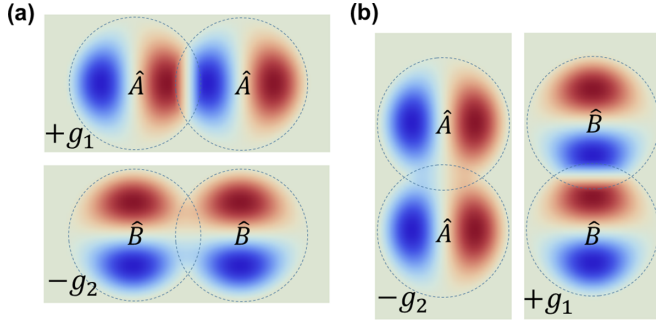


FIG. 10. Schematic drawing of the coupling of two modes \hat{A} and \hat{B} , which are defined as the (a) x - and (b) y -aligned linearly polarized modes.

From Fig. 10, the interaction Hamiltonian is given as shown in Table II.

By defining $g_S = (g_1 + g_2)/2$, $g_{AS} = (g_1 - g_2)/2$, we get

$$\begin{aligned} h_{\text{EX}-x} &= g_S(\hat{q}_{1A}\hat{q}_{2A} - \hat{q}_{1B}\hat{q}_{2B}) + g_{AS}[\hat{q}_{1A}\hat{q}_{2A} + \hat{q}_{1B}\hat{q}_{2B}], \\ h_{\text{EX}-y} &= -g_S(\hat{q}_{1A}\hat{q}_{2A} - \hat{q}_{1B}\hat{q}_{2B}) + g_{AS}[\hat{q}_{1A}\hat{q}_{2A} + \hat{q}_{1B}\hat{q}_{2B}]. \end{aligned}$$

To show that the ferromagnetic terms are dominant, we redefine \hat{q}_{2A} (and those on all the even sites) as $-\hat{q}_{2A}$ in the x axis, and \hat{q}_{2B} (and those on all the odd sites) as $-\hat{q}_{2B}$ in the y axis. The interaction Hamiltonian and the transformation becomes

$$\begin{aligned} h_{\text{EX}-x} &= -g_S(\hat{q}_{1A}\hat{q}_{2A} + \hat{q}_{1B}\hat{q}_{2B}) - g_{AS}[\hat{q}_{1A}\hat{q}_{2A} - \hat{q}_{1B}\hat{q}_{2B}], \\ h_{\text{EX}-y} &= -g_S(\hat{q}_{1A}\hat{q}_{2A} + \hat{q}_{1B}\hat{q}_{2B}) + g_{AS}[\hat{q}_{1A}\hat{q}_{2A} - \hat{q}_{1B}\hat{q}_{2B}], \\ q_{1A} &= \hat{q}_{1A} \cos \rho - \hat{q}_{1B} \sin \rho, \quad q_{1B} = \hat{q}_{1A} \sin \rho + \hat{q}_{1B} \cos \rho, \\ q_{2A} &= \hat{q}_{2A} \cos \rho + \hat{q}_{2B} \sin \rho, \quad q_{2B} = -\hat{q}_{2A} \sin \rho + \hat{q}_{2B} \cos \rho, \end{aligned}$$

from which we obtain

$$\begin{aligned} h_{\text{EX}-x} &= -g_S \cos 2\rho (q_{1A}q_{2A} + q_{1B}q_{2B}) - g_{AS}(q_{1A}q_{2A} - q_{1B}q_{2B}) \\ &\quad - g_S \sin 2\rho (q_{1B}q_{2A} - q_{1A}q_{2B}), \\ h_{\text{EX}-y} &= -g_S \cos 2\rho (q_{1A}q_{2A} + q_{1B}q_{2B}) + g_{AS}(q_{1A}q_{2A} - q_{1B}q_{2B}) \\ &\quad - g_S \sin 2\rho (q_{1B}q_{2A} - q_{1A}q_{2B}). \end{aligned}$$

TABLE II. Interaction Hamiltonian of two membrane resonators.

x axis	$h_{\text{EX}-x} = g_1 \hat{q}_{1A} \hat{q}_{2A} - g_2 \hat{q}_{1B} \hat{q}_{2B}$	$g_1 > 0, g_2 > 0$
y axis	$h_{\text{EX}-y} = -g_2 \hat{q}_{1A} \hat{q}_{2A} + g_1 \hat{q}_{1B} \hat{q}_{2B}$	

By applying rotating wave approximation, we get

$$\begin{aligned} h_{\text{EX}-x} &= -\frac{g_S}{2} [\cos 2\rho (c_{1A}c_{2A} + s_{1A}s_{2A} + c_{1B}c_{2B} + s_{1B}s_{2B}) \\ &\quad + \sin 2\rho (c_{1B}c_{2A} + s_{1B}s_{2A} - c_{1A}c_{2B} - s_{1A}s_{2B})] \\ &\quad - \frac{g_{AS}}{2} (c_{1A}c_{2A} + s_{1A}s_{2A} - c_{1B}c_{2B} - s_{1B}s_{2B}), \\ h_{\text{EX}-y} &= -\frac{g_S}{2} [\cos 2\rho (c_{1A}c_{2A} + s_{1A}s_{2A} + c_{1B}c_{2B} + s_{1B}s_{2B}) \\ &\quad + \sin 2\rho (c_{1B}c_{2A} + s_{1B}s_{2A} - c_{1A}c_{2B} - s_{1A}s_{2B})] \\ &\quad + \frac{g_{AS}}{2} (c_{1A}c_{2A} + s_{1A}s_{2A} - c_{1B}c_{2B} - s_{1B}s_{2B}). \quad (15) \end{aligned}$$

The second terms in brackets give the expression (10) in the main text. Next, we apply the parametric coupling modulation at ω_0 ,

$$\begin{aligned} g_1 &= g_{10} + g_{1p} \cos 2\omega_0 t, \quad g_2 = g_{20} + g_{2p} \cos 2\omega_0 t, \\ g_{S0} &= (g_{10} + g_{20})/2, \quad g_{AS0} = (g_{10} - g_{20})/2, \\ g_{Sp} &= (g_{1p} + g_{2p})/2, \quad g_{ASp} = (g_{1p} - g_{2p})/2. \end{aligned}$$

Then, the interaction can be divided into static and parametric terms,

$$h_{\text{EX}-x} = h_{\text{EX}0-x} + h_{\text{EX}p-x}, \quad h_{\text{EX}-y} = h_{\text{EX}0-y} + h_{\text{EX}p-y}.$$

The first terms are identical to (15). The second terms, i.e., the parametric coupling, are

$$\begin{aligned} h_{\text{EX}p-x} &= -\frac{g_{Sp}}{4} [\cos 2\rho (c_{1A}c_{2A} - s_{1A}s_{2A} + c_{1B}c_{2B} - s_{1B}s_{2B}) \\ &\quad + \sin 2\rho (c_{1B}c_{2A} - s_{1B}s_{2A} - c_{1A}c_{2B} + s_{1A}s_{2B})] \\ &\quad - \frac{g_{ASp}}{4} (c_{1A}c_{2A} - s_{1A}s_{2A} - c_{1B}c_{2B} + s_{1B}s_{2B}), \\ h_{\text{EX}p-y} &= -\frac{g_{Sp}}{4} [\cos 2\rho (c_{1A}c_{2A} - s_{1A}s_{2A} + c_{1B}c_{2B} - s_{1B}s_{2B}) \\ &\quad + \sin 2\rho (c_{1B}c_{2A} - s_{1B}s_{2A} - c_{1A}c_{2B} + s_{1A}s_{2B})] \\ &\quad + \frac{g_{ASp}}{4} (c_{1A}c_{2A} - s_{1A}s_{2A} - c_{1B}c_{2B} + s_{1B}s_{2B}). \quad (16) \end{aligned}$$

The second terms in the brackets of (16) give the expression (11) by replacing $g_{Sp} \rightarrow g_{pc}$. We used these full expressions of (15) and (16) in the numerical simulation shown in Fig. 7.

[1] N. Manton and P. Sutcliffe, *Topological Solitons* (Cambridge University Press, Cambridge, UK, 2004).

[2] T. Dauxois and M. Peyrard, *Physics of Solitons* (Cambridge University Press, Cambridge, UK, 2006).

[3] J. Rubinstein, Sine-Gordon equation, *J. Math. Phys.* **11**, 258 (1970).

[4] T. H. R. Skyrme, A unified field theory of mesons and baryons, *Nucl. Phys.* **31**, 556 (1962).

- [5] A. N. Bogdanov and U. K. Rossler, Chiral symmetry breaking in magnetic thin films and multilayers, *Phys. Rev. Lett.* **87**, 037203 (2001).
- [6] U. K. Rossler, N. Bogdanov, and C. Pfleiderer, Spontaneous skyrmion ground states in magnetic materials, *Nature (London)* **442**, 797 (2006).
- [7] S. Mühlbauer, B. Binz, F. Jonietz, C. Pfleiderer, A. Rosch, A. Neubauer, R. Georgii, and P. Böni, Skyrmion lattice in a chiral magnet, *Science* **323**, 915 (2009).
- [8] N. Nagaosa and Y. Tokura, Topological properties and dynamics of magnetic skyrmions, *Nat. Nanotechnol.* **8**, 899 (2013).
- [9] A. Fert, N. Reyren, and V. Cros, Magnetic skyrmions: Advances in physics and potential applications, *Nat. Rev. Mater.* **2**, 17031 (2017).
- [10] B. Gobel, I. Mertig, and O. A. Tretiakov, Beyond skyrmions: Review and perspectives of alternative magnetic quasiparticles, *Phys. Rep.* **895**, 1 (2021).
- [11] I. Dzyaloshinsky, A thermodynamic theory of “weak” ferromagnetism of antiferromagnetics, *J. Phys. Chem. Solids* **4**, 241 (1958).
- [12] T. Moriya, Anisotropic superexchange interaction and weak ferromagnetism, *Phys. Rev.* **120**, 91 (1960).
- [13] A. Fert and P. M. Levy, Role of anisotropic exchange interactions in determining the properties of spin-glasses, *Phys. Rev. Lett.* **44**, 1538 (1980).
- [14] F. Jonietz *et al.*, Spin transfer torques in MnSi at ultralow current densities, *Science* **330**, 1648 (2010).
- [15] X. Z. Yu, N. Kanazawa, W. Z. Zhang, T. Nagai, T. Hara, K. Kimoto, Y. Matsui, Y. Onose, and Y. Tokura, Skyrmion flow near room temperature in an ultralow current density, *Nat. Commun.* **3**, 988 (2012).
- [16] A. Fert, V. Cros, and J. Sampaio, Skyrmions on the track, *Nat. Nanotechnol.* **8**, 152 (2013).
- [17] R. Tomasello, E. Martinez, R. Zivieri, L. Torres, M. Carpentieri, and G. Finocchio, A strategy for the design of skyrmion race-track memories, *Sci. Rep.* **4**, 6784 (2014).
- [18] X. Zhang, M. Ezawa, and Y. Zhou, Magnetic skyrmion logic gates: Conversion, duplication and merging of skyrmions, *Sci. Rep.* **5**, 9400 (2015).
- [19] G. Finocchio, M. Ricci, R. Tomasello, A. Giordano, M. Lanuzza, V. Puliafito, P. Burrascano, B. Azzarboni, and M. Carpentieri, Skyrmion based microwave detectors and harvesting, *Appl. Phys. Lett.* **107**, 262401 (2015).
- [20] F. Garcia-Sanchez, N. Reyren, J. Sampaio, V. Cros, and J.-V. Kim, Askymion-based spin-torque nano-oscillator, *New J. Phys.* **18**, 075011 (2016).
- [21] K. Wang, Y. Huang, X. Zhang, and W. Zhao, Skyrmion-electronics: An overview and outlook, *Proc. IEEE* **104**, 2040 (2016).
- [22] S. L. Sondhi, A. Karlhede, S. A. Kivelson, and E. H. Rezayi, Skyrmions and the crossover from the integer to fractional quantum hall effect at small zeeman energies, *Phys. Rev. B* **47**, 16419 (1993).
- [23] H. Fertig, L. Brey, R. Cote, and A. H. MacDonald, Charged spin-texture excitations and the Hartree-Fock approximation in the quantum hall effect, *Phys. Rev. B* **50**, 11018 (1994).
- [24] S. E. Barrett, G. Dabbagh, L. N. Pfeiffer, K. W. West, and R. Tycko, Optically pumped nmr evidence for finite-size skyrmions in gaas quantum wells near landau level filling $\nu = 1$, *Phys. Rev. Lett.* **74**, 5112 (1995).
- [25] T.-L. Ho, Spinor Bose condensates in optical traps, *Phys. Rev. Lett.* **81**, 742 (1998).
- [26] T. Ohmi and K. Machida, Bose-einstein condensation with internal degrees of freedom in alkali atom gases, *J. Phys. Soc. Jpn.* **67**, 1822 (1998).
- [27] L. S. Leslie, A. Hansen, K. C. Wright, B. M. Deutsch, and N. P. Bigelow, Creation and detection of Skyrmions in a Bose-Einstein condensate, *Phys. Rev. Lett.* **103**, 250401 (2009).
- [28] T. Ozawa *et al.*, Topological photonics, *Rev. Mod. Phys.* **91**, 015006 (2019).
- [29] Y. Ota, K. Takata, T. Ozawa, A. Amo, Z. Jia, B. Kante, M. Notomi, Y. Arakawa, and S. Iwamoto, Active topological photonics, *Nanophotonics* **9**, 547 (2020).
- [30] V. Peano, M. Houde, C. Brendel, F. Marquardt, and A. A. Clerk, Topological phase transitions and chiral inelastic transport induced by the squeezing of light, *Nat. Commun.* **7**, 10779 (2016).
- [31] Z. Wang, Y. Chong, J. D. Joannopoulos, and M. Soljačić, Observation of unidirectional backscattering-immune topological electromagnetic states, *Nature (London)* **461**, 772 (2009).
- [32] V. Peano, C. Brendel, M. Schmidt, and F. Marquardt, Topological phases of sound and light, *Phys. Rev. X* **5**, 031011 (2015).
- [33] J. Cha, K. W. Kim, and C. Daraio, Experimental realization of on-chip topological nanoelectromechanical metamaterials, *Nature (London)* **564**, 229 (2018).
- [34] I. Kim, S. Iwamoto, and Y. Arakawa, Topologically protected elastic waves in one-dimensional phononic crystals of continuous media, *Appl. Phys. Express* **11**, 017201 (2018).
- [35] H. Ge, X.-Y. Xu, L. Liu, R. Xu, Z.-K. Lin, S.-Y. Yu, M. Bao, J.-H. Jiang, M.-H. Lu, and Y.-F. Chen, Observation of acoustic Skyrmions, *Phys. Rev. Lett.* **127**, 144502 (2021).
- [36] L. Cao, S. Wan, Y. Zeng, Y. Zhu, and B. Assouar, Observation of phononic skyrmions based on hybrid spin of elastic waves, *Sci. Adv.* **9**, eadf3652 (2023).
- [37] L. Du, A. Yang, A. V. Zayats, and X. Yuan, Deep-subwavelength features of photonic skyrmions in a confined electromagnetic field with orbital angular momentum, *Nat. Phys.* **15**, 650 (2019).
- [38] Q. Zhang, Z. Xie, L. Du, P. Shi, and X. Yuan, Bloch-type photonic skyrmions in optical chiral multilayers, *Phys. Rev. Res.* **3**, 023109 (2021).
- [39] S. Tsesses, E. Ostrovsky, K. Cohen, B. Gjonaj, N. H. Lindner, and G. Bartal, Optical skyrmion lattice in evanescent electromagnetic fields, *Science* **361**, 993 (2018).
- [40] H. Yamaguchi and S. Hourii, Generation and propagation of topological solitons in a chain of coupled parametric-micromechanical-resonator arrays, *Phys. Rev. Appl.* **15**, 034091 (2021).
- [41] S. Rahav, I. Gilary, and S. Fishman, Effective hamiltonians for periodically driven systems, *Phys. Rev. A* **68**, 013820 (2003).
- [42] T. Oka and S. Kitamura, Floquet engineering of quantum materials, *Annu. Rev. Condens. Matter Phys.* **10**, 387 (2019).
- [43] S. Yin, E. Galiffi, and A. Alù, Floquet metamaterials, *eLight* **2**, 8 (2022).
- [44] M. Marthaler and M. I. Dykman, Switching via quantum activation: A parametrically modulated oscillator, *Phys. Rev. A* **73**, 042108 (2006).
- [45] A. Bogdanov and A. Hubert, Thermodynamically stable magnetic vortex states in magnetic crystals, *J. Magn. Magn. Mater.* **138**, 255 (1994).

- [46] J. H. Han, J. Zang, Z. Yang, J.-H. Park, and N. Nagaosa, Skyrmion lattice in a two-dimensional chiral magnet, *Phys. Rev. B* **82**, 094429 (2010).
- [47] H. Okamoto, A. Gourgout, C. -Y. Chang, K. Onomitsu, I. Mahboob, E. Y. Chang, and H. Yamaguchi, Coherent phonon manipulation in coupled mechanical resonators, *Nat. Phys.* **9**, 480 (2013).
- [48] D. Hatanaka, I. Mahboob, K. Onomitsu, and H. Yamaguchi, Phonon waveguides for electromechanical circuits, *Nat. Nanotechnol.* **9**, 520 (2014).
- [49] See Supplemental Material at <http://link.aps.org/supplemental/10.1103/PhysRevResearch.5.043076> for a stop-motion animation of Bloch skyrmion dynamics formed by a membrane resonator array.
- [50] S. Adachi, *Physical Properties of III-V Semiconductor Compounds* (John Wiley & Sons, Inc., New York, United States, 1992), Sec. 5.2.
- [51] S. Schmid, L. G. Villanueva, and M. L. Roukes, *Fundamentals of Nanomechanical Resonators* (Springer International Publishing, Switzerland, 2016), Sec. 4.5.1.